UV and aerosol climatology based on simulations and measurements by satellites and ground station

Yi-Chun Chen

Dissertation for the degree of Philosophiae Doctor (PhD)

Department of Physics and Technology
University of Bergen

December 2012

Acknowledgements

I would like to express my great appreciation to my supervisor Prof. Jakob Stamnes and co-supervisor Prof. Øyvind Frette for all the supports in the past three and a little be more years. Especially thank Jakob for enduring my poor English and correcting the articles patiently and carefully. Also thank Øyvind for concerning about my daily life and offering his leg for me to kick when I need to release some pressure, although I have never thought the offer is for real. I am grateful for all the helps from Børge Hamre. I always go to him with a lot of odd problems, and he always willing to solve them. I would like to express my gratitude to Prof. Knut Stamnes and his group members in Stevens Institute of Technology, NJ, USA, for helping me on scientific side and also on the one month stay in Hoboken. I would like to thank all the members of Optics and atomic physics group in Department of Physics and Technology, University of Bergen. I feel very lucky to share a corridor with them, because they never parsimonious to show me their friendly smiles and warm greetings. Particularly thank Prof. Jan Petter Hansen for introducing me the sporty side of Norwegian and encouraging me to be the Ski Champion of Taiwan.

I would like to thank my friends Patty, Yu-Mei, and XiaoZi for making me numberless delicious dishes and warm concerns. They not just warmed my stomach but also warmed my heart. I enjoyed every food experiment we have done together. I would like to thank all the friends I met in Norway. It is amazing that we come from different places of the world and then meet each other in this raining city. Maybe we will be apart soon, but I will cherish our friendship and remember them all.

Finally, I would like to dedicate this thesis to my beloved family. Along the way, I have never felt I am far away from them, because they are in my heart all the time.

Yi-Chun Chen
Bergen, the raining city.

Abstract

Solar radiation (200–4,000 nm) is very important for the climate system on Earth. It provides heat and drives the photosynthesis in plants to fuel all life. It plays a major role in the original synthesis of biomolecules and in the evolution of life on Earth. Many acute and chronic health damages to the skin, eyes, and immune system of humans are caused by prolonged exposure to solar UV radiation. The most well-known impacts on human health from exposure to UV radiation are skin aging, sunburn, and skin cancer. The atmosphere has a big impact on the transfer of energy between the Sun and the Earth's surface. It serves to maintain thermal equilibrium and to control the climate.

The UV irradiance decreases strongly at wavelengths below 330 nm due to absorption by atmospheric ozone. This absorption occurs in the UV-A and UV-B regions (280–400 nm), which is also called biologically active dose rate region. Although the absorption of UV-B radiation only is a small part of the total absorption in the UV spectral range, a small increment of UV-B radiation can lead to substantial biological effects because of higher exposure to radiation at shorter wavelengths.

The UV index (UVI), the total ozone column amount (TOCA), and the cloud modification factor (CMF) at four sites on the Tibetan Plateau (TP) have been determined in this study by use of multichannel moderate-bandwidth filter instruments at the ground in the period 2008–2010. The geographical locations and altitudes of these sites are 29.66°N, 94.37°E, 2,995 m for Linzhi; 29.65°N, 91.18°E, 3,683 m for Lhasa; 28.66°N, 87.13°E, 4,335 m for Tingri; and 31.47°N, 92.06°E, 4,510 m for Nagchu. TP is located in a northern mid-latitude region and is the largest and highest plateau area in the world with an average elevation of more than 4,000 m. The UVI on the TP can reach up to 20.6 in one-minute measurement during summer time, while 10 is an exceptionally high value for northern mid-latitudes. The annual mean TOCA values were found to be similar around 260-264 Dobson units (DU) in Lhasa, Linzhi, and Nagchu, and 252 DU in Tingri. The CMF values were found to be 0.70 for Linzhi, 0.83 for Lhasa, 0.92 for Tingri, and 0.70 for Nagchu. The effects of altitude, latitude and TOCA values on the UVI have been investigated in this thesis through the use of a radiative transfer (RT) model. The result shows that the high altitude of the TP combined with low latitude and low TOCA values caused the high UVI values observed during our investigation.

Atmospheric aerosols are suspensions of solid or liquid particles in air, and are often observed as dust, smoke, and haze. They have different compositions, sizes, shapes, and optical properties and varying atmospheric lifetimes. Aerosol particle sizes range from a few nanometers to a few tens of micrometers. The radiative climate forcing

of the Earth is affected by aerosols. The direct effect of aerosols is caused by large aerosols particles, which can absorb part of the incoming solar radiation and scatter another part back to space. Absorption tends to heat the planet and backscattering tends to cool it. The indirect effect of aerosols is due to small aerosol particles, which can act as cloud condensation nuclei (CCN) and thus increase the amounts of clouds and modify their microphysical and radiative properties. Understanding optical properties of aerosols is important in investigations of climate change, since aerosols have a major impact on the radiative energy balance.

In this study, we have compared aerosol loadings in Northern Norway and Svalbard based on data from AERONET (AErosol RObotic NETwork) stations at Andenes (69 °N, 16 °E, 379 m altitude) and Hornsund (77 °N, 15°E, 10 m altitude) for the period 2008–2010. The three-year annual mean values for the aerosol optical thickness at 500 nm τ_{500} at Andenes and Hornsund were found to be 0.11 and 0.10, respectively. At Hornsund, there was less variation of the monthly mean value of τ_{500} than at Andenes. The annual mean values of the Ångström exponent α at Andenes and Hornsund were found to be 1.18 and 1.37, respectively. At Andenes and Hornsund α was found to be larger than 1.0 in 68% and 93% of the observations, respectively, indicating that fine-mode particles were dominating at both sites. Both sites had a similar seasonal variation of the aerosol size distribution although one site is in an Arctic area while the other site is in a sub-arctic area. We used information retrieved from AERONET measurements about aerosol microphysical properties, i.e. refractive index and size distribution of aerosol particles (which were assumed to be spherical), to obtain solutions of Maxwell's equations for scattering by a size distribution of spherical particles (Mie scattering), and thus provide Inherent Optical Properties (IOPs) required for RT computations (AOT, single-scattering albedo, and scattering phase function). As additional inputs to RT computations, we used geometry parameters (e.g. altitude and solar zenith angle) from the AERONET site at Andenes (69 °N, 16 °E, 379 m altitude) together with ozone data from OMI and different types of surface albedo. We used a radiative transfer (RT) model for coupled atmosphere-ocean systems, in which the radiative coupling between the atmosphere and the ocean is accounted for.

The mean value of the aerosol optical thickness at 500 nm derived from AERONET measurements was found to be very close to the mean value obtained from RT modeling with IOP inputs obtained from Mie-scattering computations in conjunction with aerosol size distributions and wavelength-dependent refractive index as derived from AERONET measurements. Changes in the aerosol radiative forcing (ARF) due to changes in the surface reflectance was studied by considering six different types of surfaces. Although the ARF at the BOA retrieved from the AERONET algorithm showed good agreement with that computed by C-DISORT, the spectral irradiances at BOA inferred from AERONET measurements did not agree so well with those obtained from C-DISORT computations. Overall, the ARF values derived from AERONET measurements were smaller than those obtained from C-DISORT computations at TOA, but were larger at BOA.

We also analyzed UVI, TOCA, and aerosol index (AI) values based on measurements by satellite instruments. To that end, we used more than three decades of global

data (1979–2012) for tropospheric aerosols from the Total Ozone Mapping Spectrometer (TOMS) and the Ozone Monitoring Instrument (OMI). These instruments provided backscattered radiance measurements in the wavelength range from 331 to 380 nm, which we used to determine the aerosol climatology and to investigate the effects of the AI on the UVI in two coastal land areas [Serrekunda (13.28°N, 16.34°W, at sea level), Gambia and Dar-es-Salaam (6.8°S, 39.26°W, at sea level), Tanzania] and one inland area [Kampala (0.19°N, 32.34°E, 1200 m altitude), Uganda]. We found heavy aerosol loadings to occur in the dry seasons at all these three locations. Also, we made a comparison of UVI values inferred from satellite measurements with those obtained from radiative transfer modeling.

The RT code used for radiative transfer computations in this study is based on the multiple-stream, multiple scattering DIScrete Ordinate Radiative Transfer model (DISORT). This RT code, C-DISORT, applies to a *coupled* system, such as an atmosphere-ocean system or an atmosphere-snow-ice-ocean system, for use by researchers in the ocean optics, climate research, and remote sensing communities. The C-DISORT code allows for a user-specified number of layers in the coupled system to adequately resolve the vertical variation in the inherent optical properties (IOPs), and it computes apparent optical properties (AOPs), such as the upward and downward irradiances, the scalar irradiance, and the diffuse attenuation coefficients at user-specified optical depths in the coupled system. It also computes radiances in user-specified directions at user-specified optical depths in a coupled system.

In future work, we plan to use the C-DISORT code to perform simultaneous retrieval of aerosol and marine parameters in waters along the Norwegian coast based on (i) data collected by hyperspectral radiance and irradiance sensors onboard ships of opportunity, such as the Norwegian Coastal Express (Hurtigruten), (ii) forward computations using C-DISORT, and (iii) inversions based on optimal estimation theory.

List of papers

1. G. Norsang, Y.-C. Chen, N. Pingcuo, A. Dahlback, Ø. Frette, B. Kjeldstad, B. Hamre, K. Stamnes, and J. J. Stamnes, *Comparison of ground-based measurements of solar UV radiation at four sites on the Tibetan Plateau*, submitted to J. Geophys. Res., 2012.

2. Y.-C. Chen, B. Hamre, Ø. Frette, and J. J. Stamnes, *Climatology of aerosol optical properties in Northern Norway and Svalbard*, Atmos. Meas. Tech. Discuss., **5**, 7619–7640, 2012.

3. T. Ssenyonga, Y.-C. Chen, A. Dahlback, A. Steigen, W. Okullo, Ø. Frette, D. Muyimbwa, and J. J. Stamnes, *Aerosols in coastal and inland areas in the equatorial African Belt*, to be submitted to J. Atmos. Sci.

4. Y.-C. Chen, B. Harmre, S. Stamnes, Ø. Frette, K. Stamnes, and J. J. Stamnes, *Sensitivity analyses of aerosol radiative forcing in Northern Norway*, to be submitted.

Contents

List of Figures

List of Tables

Chapter 1

Introduction

1.1 Atmosphere of the Earth

Th Earth is surrounded by an atmosphere, which is a gaseous medium enveloping the globe. The atmosphere plays a major role in the transfer of energy between the Sun and the Earth's surface. It serves to maintain thermal equilibrium and to control the climate. In accordance with its thermal characteristics, chemical composition, movement, and density, the atmosphere has been identified to have five distinct layers, which are bounded by "pauses", at which large changes occur. The layers most important to life on Earth is the two layers farthest away from its surface [1].

The lowest layer of the atmosphere is the *troposphere*, which interacts with living organisms on Earth. The troposphere begins at the Earth's surface and extends upwards to between 7 and 20 km. The thickness of the troposphere depends on latitude and season. At the poles it is only 7 km thick, and it increases with decreasing latitude until it reaches its maximum thickness at equator. Cold conditions in winter time lead to a smaller thickness of the troposphere due to less convection. The density and temperature of gases decrease with altitude in the atmosphere. Air becomes thinner and the temperature drops to -50°C at the top of the troposphere. About 80% of the air mass, and 99% of water vapor and aerosols are contained in the tropospheric layer, where weather phenomena, such as rainfall, snowfall, and cloud formation, occur.

The layer above the troposphere is called the *stratosphere*, and the boundary between the troposphere and the stratosphere is called the *tropopause*. The stratosphere ends at an altitude of 50 km. Supersonic jet air planes usually fly above the tropopause, because the air flow in the stratosphere is very stable. But subsonic commercial airliners usually fly in the troposphere. However, the maximum altitudes of aircraft and weather balloons are within the stratosphere, due to thinner air masses high up in the troposphere. Air at the top of the stratosphere is roughly one thousand times thinner than at sea level. Ozone is relatively abundant in the stratosphere and has a high concentration in the layer between 15 and 35 km above sea level (see Figure 1.1) [2]. About 90% of the total ozone column amount (TOCA) in the atmosphere resides in the stratosphere, where it absorbs ultraviolet radiation and prevents it from reaching the Earth's surface. The remaining part (about 10%) of the TOCA is found in the troposphere (see Section 1.3) [3, 4].

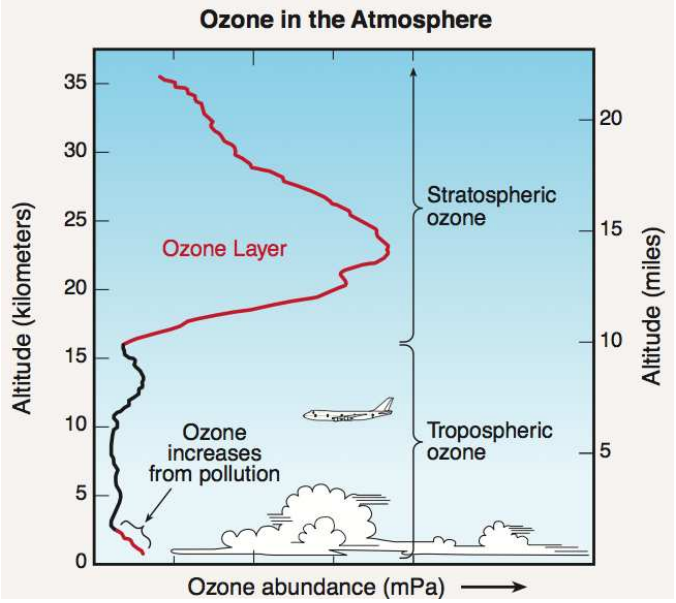

Figure 1.1: *The concentration of ozone in the atmosphere* [2]. Ozone abundances are shown as the pressure of ozone at each altitude in the unit of "milli-Pascal" (mPa) (100 million mPa = atmospheric sea-level pressure).

1.2 Ultraviolet Solar Radiation

Solar radiation (200–4,000 nm) is very important for the climate system on Earth. It provides heat and drives the photosynthesis in plants to fuel all life. It played an indispensable role in the original synthesis of biomolecules and in the evolution of life on Earth. Ultraviolet (UV) radiation is in the wavelength range 200–400 nm, between *X* rays and visible light. Solar radiation at short wavelengths have high energy and may cause health damages. The penetration depth of light into human skin increases with the wavelength, and may reach depths that are invisible to the human eye. Many acute and chronic health damages to the skin, eyes, and immune system of humans are caused by prolonged exposure to solar UV radiation. The most well-known impacts on human health from exposure to UV radiation are skin aging, sunburn, skin cancer, and DNA damage [5–10]. UV radiation has also been used in the water cleansing industry to provide safe drinking water, since it is very effective against some types of pathogenic micro-organisms [11]. Overall, UV radiation is indispensable to living organisms on Earth, but it has both benefits and disadvantages.

The UV spectral range is divided into three different parts, UV-C (200–280 nm), UV-B (280–315 nm), and UV-A (315–400 nm).

- **UV-C**: UV-C radiation is totally absorbed by oxygen and atmospheric ozone, and is almost never observed at the surface of the Earth. But it is commonly made artificially to prevent contaminants caused by organic or carbon-based compounds in indoor environments. High intensities of UV exposure in the wavelength range 240–280 nm destroy such compounds effectively. The injury caused by UV-C radiation to humans is extremely painful but lasts only one day or two. Excessive exposure to UV-C causes skin cancers and DNA damages, while chronic exposures to acute intense UV-C can lead to cataract formation and retinal damage. However, no significant irradiation of humans on Earth results from natural sources, since UV-C is strongly attenuated by atmospheric gases [12–14].

- **UV-B**: More than 90% of the UV-B radiation is absorbed by atmospheric ozone, so that less than 10% of the UV-B radiation reaches the surface. It is an important element for humans in the synthesis of vitamin D. However, overexposure to UV-B radiation may lead to erythema (sunburn), DNA damage, and skin cancer [12–14]. Therefore, the high concentration of ozone in the stratosphere is a key factor in blocking harmful UV radiation from reaching living organisms on Earth [15]. The research of Caldwell et al. [16] shows that increased solar UV radiation due to stratospheric ozone depletion may affect terrestrial ecosystems, such as plants and microorganisms. Also, effects of increased UV-B radiation levels may be related to other climate changes, such as increased temperature and increased levels of carbon dioxide, which may alter the UV-B response, especially for plants [17–19]. But clouds and aerosols also cause a large variability in the amount of UV-B radiation reaching the surface of the Earth, so that UV-B radiation levels on the ground are not just affected by ozone.

- **UV-A**: UV-A radiation accounts for the major part of the UV irradiance that reaches the surface of the Earth. Only small amounts of the solar UV-A radiation is absorbed by atmospheric ozone. Also, as mentioned above, the radiation in the UV-A range of the spectrum helps humans to synthesis vitamin D. But it leads to DNA damages and skin toughening, and may cause suppression of the immune system and cataract formation [12–15, 20].

1.2.1 Erythemal UV irradiance

The UV irradiance decreases strongly at wavelengths below 330 nm, due to a absorption by atmospheric ozone. This absorption occurs in the UV-A and UV-B regions (280–400 nm). Although the absorption of UV-B radiation only is a small part of the total absorption in the UV spectral range, a small increment of UV-B radiation can lead to substantial biological effects because of higher exposure to radiation at shorter wavelengths. To estimate biological effects, one can multiply the UV irradiance with a spectral sensitivity function (action spectrum) [15], and integrate the product over the UV spectral range. A theoretical estimation made by Madronich and Flock [21] showed the biologically active dose rate to be strongly affected by atmospheric ozone. Figure 1.2 shows the spectral irradiance $F(\lambda)$ and the erythemal action spectrum $B(\lambda)$ given by Mckinlay and Diffey [22] (called $A(\lambda)$ in this thesis). The product $F(\lambda)B(\lambda)$

in Figure 1.2 is the erythemal UV irradiance. The solid and dotted lines are for TOCAs of 348 DU (Dobson Unit) and 250 DU, respectively [21]. For a common atmospheric condition at a northern mid-latitude site, the erythemal UV irradiance increases by approximately 1.1 to 1.7% for a 1.0% decrease in the TOCA [15].

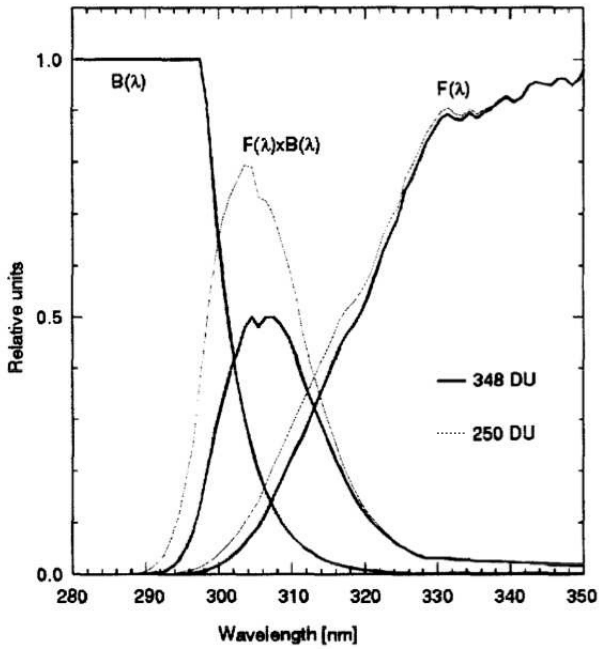

Figure 1.2: *Erythemal UV irradiance* [21].

The erythemal UV irradiance UV_{Ery} is defined by

$$\mathrm{UV}_{\mathrm{Ery}} = \int A(\lambda) F(\lambda) \, d\lambda \tag{1.1}$$

where $F(\lambda)$ is the spectral irradiance at wavelength λ, and $A(\lambda)$ is a biological action spectrum and the integral is carried out over all UV wavelengths. For erythema, the action spectrum $A(\lambda)$ employed is the widely acknowledged Commission International de l'*É*clairage (CIE) action spectrum [22].

The CIE action spectrum is defined as follows [22] (see also the line in cyan in Figure 1.3):

$$A(\lambda) = 1 \text{ for } 250 \text{ nm} \leq \lambda \leq 298 \text{ nm}; \tag{1.2}$$

$$A(\lambda) = 100.094\,(298 - \lambda) \text{ for } 298 \text{ nm} \leq \lambda \leq 328 \text{ nm}; \tag{1.3}$$

$$A(\lambda) = 100.015\,(139 - \lambda) \text{ for } 328 \text{ nm} \leq \lambda \leq 400 \text{ nm}. \tag{1.4}$$

The World Meteorological Organization (WMO) has defined a standard conversion from a CIE weighted UV irradiance or an erythemal UV irradiance value to a UV Index (UVI) by letting 25×10^{-3} W m^{-2} be equal to 1 UVI [23]. Thus, by multiplying the erythemal UV irradiance in units of W m^{-2} by 40, one obtains the UVI, which is a unit-less quantity:

$$\mathrm{UVI} = 40 \times \mathrm{UV_{Ery}} \ (\text{with } \mathrm{UV_{Ery}} \text{ given in W m}^{-2}). \tag{1.5}$$

UVI values are considered to be *Low* in the range 0–2, *Moderate* in the range 3–5, *High* in the range 6–7, *Very High* in the range 8–10, and *Extreme* in the range above 11 [24].

The highest values of the UVI occur in the tropics, where the mid day Sun is highest throughout the year, and where the TOCA values are lowest. On a clear sky day at sea level in the tropics, the UVI would normally be in the range 10–12 (2.50–3 W m^{-2}), and 10 is an exceptionally high value for northern mid-latitudes [25]. Extremely high solar UV radiation levels can be found in northern mid-latitudes as well, such as at the Tibetan Plateau, due to high altitude combined with low latitude and low TOCA values (see the discussion in Chapter 6).

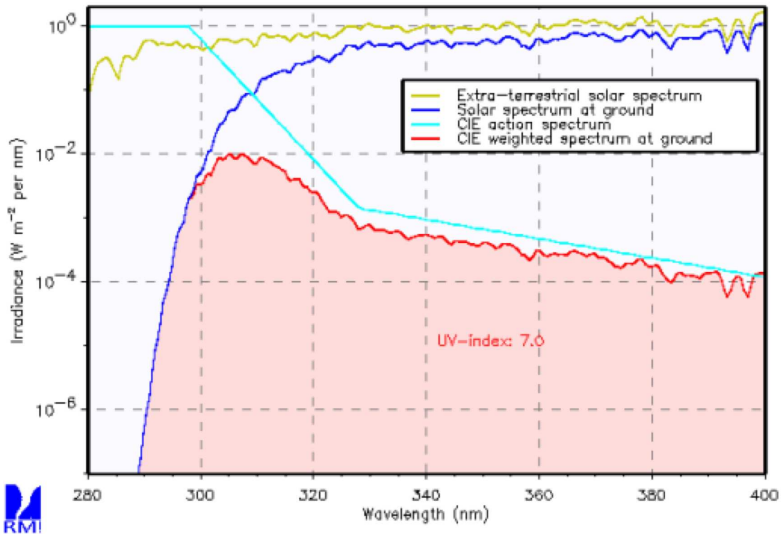

Figure 1.3: *The solar spectrum at top the atmosphere and at the surface, and the CIE weighted spectrum* [26].

Figure 1.3 shows the irradiance of the extra-terrestrial solar radiation between 280 and 400 nm (yellow line, top of the atmosphere (TOA)). The blue line represents the irradiance at the ground surface at a mid latitude site. The line in cyan is the CIE action spectrum. The solar irradiance spectrum at the ground multiplied by the CIE action spectrum is called the effective irradiance at the ground surface (red line). The integrated value of the effective irradiance between 280 and 400 nm (UV_{Ery}) multiplied by

40 is the UVI (red-shaded area) [26].

1.3 Ozone

Stratospheric ozone is the major absorber of UV radiation, protecting us from biological damages caused by overexposure of harmful UV radiation. About 90% of the total ozone column amount (TOCA) in the atmosphere is contained in the stratosphere, forming a high concentration layer between roughly 15 and 35 km above sea level (see Figure 1.1). Unlike the thickness variation of the troposphere, which is thinnest at the poles, the ozone layer in the stratosphere is thinnest in the equatorial region and becomes thicker towards to the poles. The remaining ozone (about 10%) is found in the troposphere.

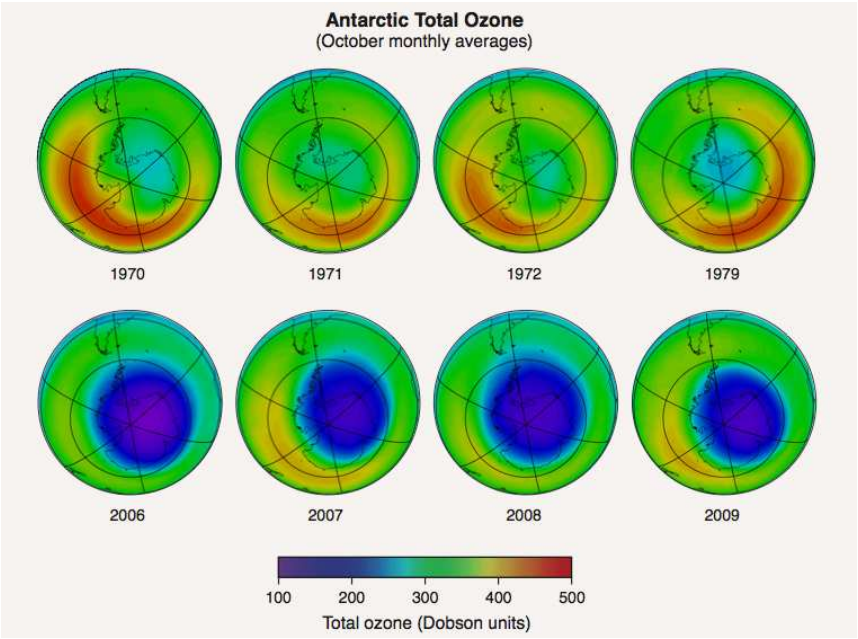

Figure 1.4: *The ozone hole over Antarctica (A series of total ozone maps derived from satellite observations)* [2].

A major loss of stratospheric ozone over Antarctica was first noticed in the 1970s by a research group from the British Antarctic Survey (BAS) [27]. Since then ozone depletion has been observed also at mid-latitudes and in the Arctic. However, the ozone depletion over Antarctica extended over a very large area, referred to as the Ozone Hole (see Figure 1.4) [2]. Nearly all ozone was destroyed over an area the size of the whole Antarctic continent. Figure 1.5 shows the measured October month average of the total ozone above the Halley Bay station in Antarctica for the period from 1961 to 2012 (Antarctic Spring is around October) [28]. No satellite data are available during the

Antarctic winter (May - July), since the South pole is in total darkness during that period. The average total ozone for the month of October had a sudden decreasing trend after about 1975. The drop in ozone levels in the stratosphere after 1975 was so dramatic that, at first, the scientists thought their instruments were faulty. By 1994 the ozone column was less than half its value during the 1970s [29, 30].

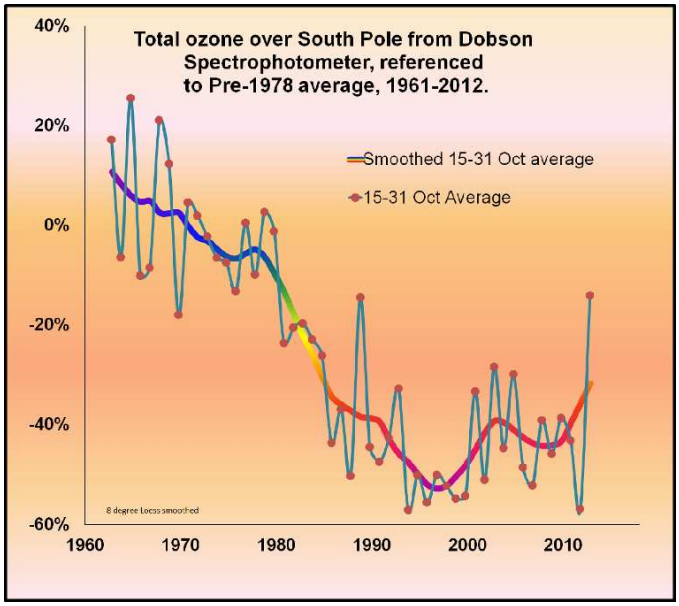

Figure 1.5: *Total ozone column over Antartica during 1961 to 2012* [28].

The chlorine from chlorofluorocarbons (CFCs) are believed to be the main man-made cause of ozone depletion in the stratosphere since chlorine from other sources, such as swimming pools, industrial plants, sea salt, and volcanoes, combine with water and will rain out of the troposphere very quickly, so that it does not reach the stratosphere. CFCs are stable, nonflammable, low in toxicity, and inexpensive to produce, and they have been widely used as refrigerants, solvents, foam blowing agents, and in many other applications. These stable CFCs do not dissolve in rain and can be driven into the stratosphere by winds. When CFCs move to stratosphere, the compounds of CFCs are broken down by strong UV radiation, and breakdown products of CFCs release molecular chlorine after chemical reactions. These chemicals in the stratosphere freeze out and form polar stratospheric clouds (PSCs), which are meteorologically isolated from air at higher latitudes (polar vortex) due to the very low temperature in the dark winter time. When sunlight returns to the polar region after the polar winter, the molecular chlorine is rapidly split into chlorine atoms which lead to a sudden loss of ozone. About over 100,000 ozone molecules will be destroyed by one chlorine atom due to its catalytic cycles, and the temperature of the lower stratosphere plays an important role [2, 31, 32].

In the Arctic, close to the North Pole, the ozone depletion is much less than in the

Antarctica because of the generally higher temperatures at high latitudes in the northern hemisphere due to the lack of a land continent at the North Pole. Consequently, less CFS chemicals freeze out to form PSCs that can absorb sunlight for chlorine activation in spring time [33]. Figure 1.6 shows changes in the minimum air temperature in the polar stratosphere between 1978 and 2010 [2]. The formation temperature of PSCs is about -78°C. Only during 1 to 2 months of a year can the temperature of the arctic atmosphere reach down to the PSC formation temperature, but over Antarctica such low temperatures can be reached during 5 to 6 months. A long-term observation of ozone depletion in the spring time over the two polar regions is shown in Figure 1.7 [2]. Ozone was found to almost disappear between 14 and 21 km in the spring of 2006 over Antarctica near the South pole (left panel). The average ozone value at the altitude for maximum ozone (16 km) during the period from 1990 to 2009 was 90% lower than the value in the period before 1980. The observations at Ny-Ålesund in the Arctic (right panel) were done from 1991 to 2009. A significant ozone depletion was found in the spring of 1996. But the ozone depletion over the Arctic was not as serious as over the Antarctica. The total ozone column amount (TOCA) is given in Dobson units (DU), while the unit for the ozone abundance in Figure 1.7 is mPa.

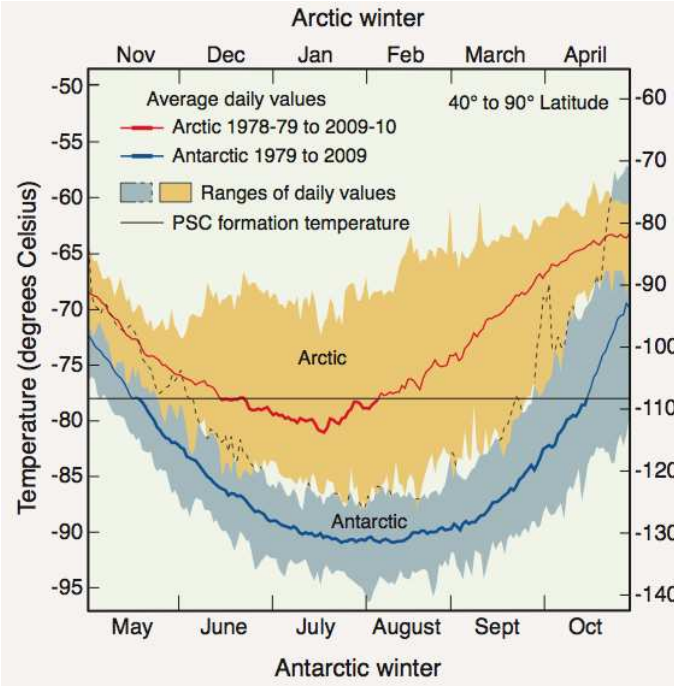

Figure 1.6: *Minimum air temperatures in the polar stratosphere during 1978 to 2010* [2].

Although the changes of UV radiation caused by tropospheric ozone are smaller then those by stratospheric ozone, tropospheric ozone absorbs UV-B radiation effectively as well, specifically in summer time at small solar zenith angles [34]. Tropospheric ozone is formed by the photochemical reaction of some pollutions, such as

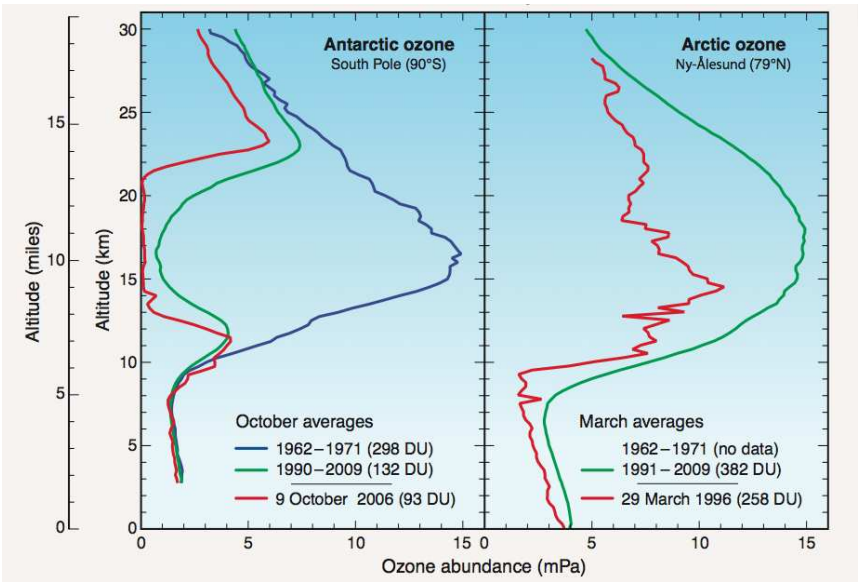

Figure 1.7: *Polar ozone depletions* [2].

nitrogen oxides and hydrocarbons, in urban and industrialized area. Ozone near the Earth's surface is considered to be bad when it is in excess of natural amounts [32].

Using satellite observations, one may separately attribute UV-B radiation changes to changes in total ozone amount (TOCA) and cloud cover [35, 36]. Between 1979 and 2008, the net increase in the erythemal UV radiation in the tropics and in regions of the Northern Hemisphere, was determined primarily by ozone depletion, since the average change in cloud cover during this period was very small. By using satellite measurements together with a simplified radiative transfer approach based on Beer's Law for both monochromatic and action spectrum weighted irradiances, one can infer that without change in cloudiness, the increase in the erythemal UV radiation due to ozone depletion at high latitudes of the Southern Hemisphere during this period would have been up to a maximum close to 9% [36]. Over a wide range of latitudes outside the tropics, the erythemal UV radiation increased by up to 6% between 1979 and 2008 [36].

1.4 Atmospheric Aerosols

Atmospheric aerosols are suspensions of solid or liquid particles in air, and are often observed as dust, smoke, and haze. They have different compositions, sizes, shapes, and optical properties and varying atmospheric lifetimes. The range of particle size is from a few nanometers to a few tens of micrometers. Table 1.1 shows typical mass concentrations and sizes of aerosols representative for urban, rural, and marine regions [37].

The climate forcing of the Earth is affected by aerosols both *directly* and *indirectly*.

Area	Concentration [μg m^{-3}]	Diameter [μm]
Urban	>100	0.03
Rural	30-50	0.07
Marine	>10	0.16

Table 1.1: *Mass concentrations and particle sizes of aerosols* [37].

The direct effect is caused by large aerosols particles, which can absorb a part of the incoming solar radiation and scatter another part of it back to space. Absorption tends to heat the planet and backscattering tends to cool it [38]. The indirect effect is due to small aerosol particles, which can act as cloud condensation nuclei (CCN) and thus increase the amounts of clouds and modify their microphysical and radiative properties. The concentrations of CCN and ice nuclei will increase with the aerosol particle concentration. For a fixed cloud liquid content, an increase in the amount of CCN will cause more cloud droplets of smaller size making clouds more reflective and longer lasting [39].

Both natural and anthropogenic (human) processes may contribute to the aerosol concentration. Natural aerosols, such as those produced by volcanoes, are present mainly in the stratosphere, whereas the lower troposphere mainly contains anthropogenic aerosols. Anthropogenic aerosols originate from urban and industrial emissions, agricultural burning, domestic fires, deforestation, and farming practices.

A summary of those aerosol processes which are most important due to their influence on climate is shown in Fig. 1.8. Key processes are: (i) the emission of primary aerosol particles directly into the atmosphere, such as desert and soil dust, smoke, volcanic ash, and sea salt and bubbles from breaking of ocean whitecaps, (ii) the emission and oxidation of aerosol precursor gases, (iii) the formation of new particles, (iv) the coagulation of particles, (v) the interactions of particles with cloud droplets, and (vi) the deposition of particles on the ground surface. The aerosol optical depth (AOD) (also called the aerosol optical thickness, AOT) of the atmosphere is one of the main characteristics of atmospheric aerosols [40].

The AOD is a dimensionless quantity, defined as the amount of the incident light that is scattered and absorbed by aerosol particles in the atmosphere. The AOD is usually measured along a vertical path through the entire height of the atmosphere. The AOD varies widely depending on atmospheric conditions and is typically much smaller for longwave radiation than for shortwave radiation. For wavelengths in the visible region, AOD values range from 0.02 to 0.2.

1.5 Atmospheric Impact

In the Third Intergovernmental Panel on Climate Change Assessment Report (IPCC TAR 2001) [41], a comparison is given (see Fig. 1.9) of the change in impact various

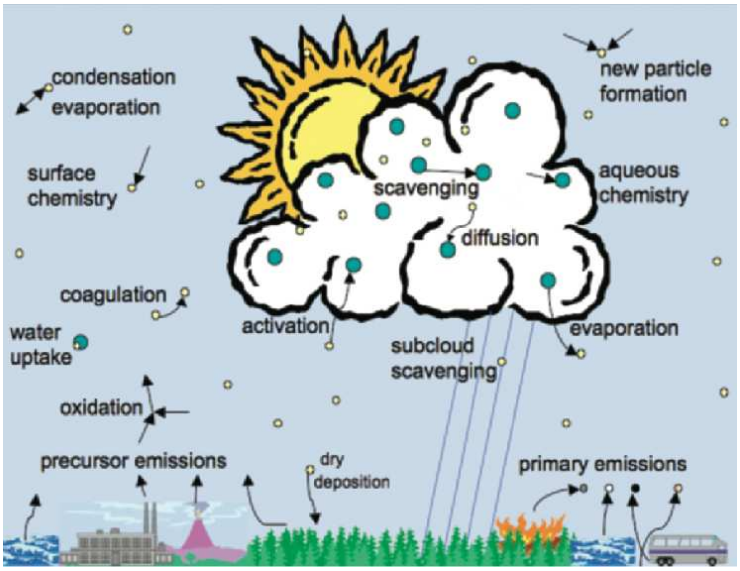

Figure 1.8: *The influence of aerosol processes on climate* [40].

factors have had on the climate from year 1750 to year 2000. The wide, colored bars in Figure 1.9 represent the quantified radiative forcing factors. According to IPCC TAR 2001, radiative forcing is defined as the net (downward minus upward) irradiance (solar plus long-wave) change at the tropopause after a new thermal equilibrium state has been established in the stratosphere [41].

Figure 1.9 indicates that the change since the pre-industrial era in the radiative forcing due to increase in anthropogenic greenhouse gases is positive (warming) with a small uncertainty range. Radiative forcing is measured in watts per square meter of surface, and it is a direct measure of the impact that recent human activities has had on the energy balance of the Earth's climate system. It includes the addition of greenhouse gases to the atmosphere as well as the impact of deforestation, which changes the reflectivity of the Earth's surface. IPCC TAR 2001 uses 1750, which was at the beginning of the world industrialization, as its reference year and computes radiative forcing in relation to that reference. Further, Figure 1.9 shows that the change in the radiative forcing during this period due to direct effects of aerosols is negative (cooling) but fairly small, whereas the corresponding change due to indirect effects of aerosols may be negative and large but with a large uncertainty range. This large uncertainty shows that the scientific understanding of the impact of aerosols and clouds on the climate is limited. Thus, currently there is a large uncertainty about the direct aerosol effect on radiation and an even larger uncertainty about the indirect aerosol effect on clouds [41].

Figure 1.10 shows the influence of various factors on the climate from year 1750 to year 2005 according to the IPCC AR4 2007 [42] report. Compared to the results of IPCC TAR 2001, the uncertainties of the various factors are reduced in IPCC AR4 2007, but the assessed levels of scientific understanding are still designated to be

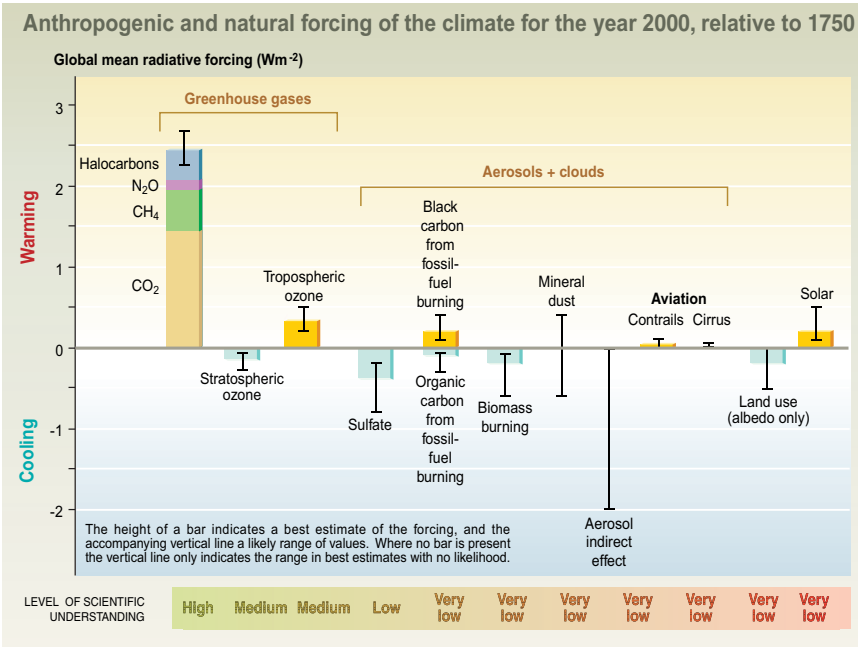

Figure 1.9: *The influence of various factors on the climate from year 1750 to year 2000* [41].

"Medium Low" and "Low" for the direct and indirect climate forcing, respectively. Also the assessed levels of scientific understanding of the climate impacts of ozone and solar radiation are not good enough [41, 42].

The greatest uncertainties in the understanding of the climate system are due to radiative forcing by clouds and aerosols [42]. To reduce these uncertainties, Earth observations from satellites are being used since satellite instruments provide both temporal and global information about the atmospheric impact on the radiative forcing. But it is difficult to separate the surface and atmospheric contributions to the radiation measured by a satellite instrument. For that reason, several different algorithms and satellite instruments (such as MODIS [43–45], MERIS [46–48], and MISR [49, 50]) are being used to help distinguish the surface contribution from the atmospheric contribution [51].

Algorithms for deriving aerosol properties over land and water areas have been developed by many groups [44, 47, 49, 52, 53] in order to extract the aerosol contribution to the top-of-the atmosphere (TOA) radiance measured by a satellite instrument from the total contribution to the TOA radiance due to absorption and scattering also by atmospheric molecules and clouds as well as backscattering from the land or water surface. Compared to the surface backscattering, particularly over bright desert surfaces and snow-covered areas, the aerosol contribution to the TOA radiance is usually small [54].

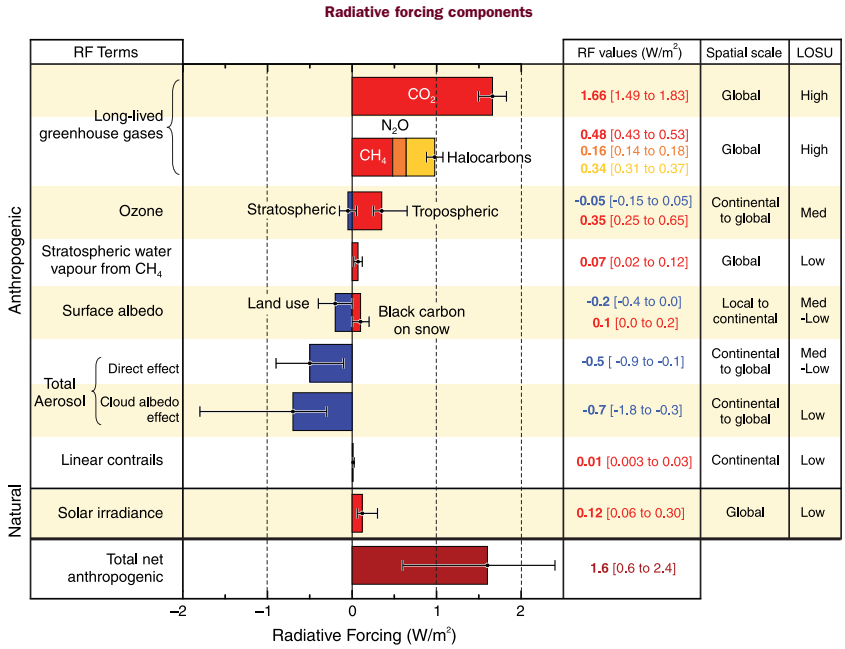

Figure 1.10: *The influence of various factors on the climate from year 1750 to year 2005* [42].

Many satellites with instrumentation for monitoring ozone changes have been launched since the 1960s. Over the past three decades, satellite images have provided both temporal and global information about the important ozone layer. The ozone instrument from which data have been used in this thesis is TOMS-OMI (see Section 2.2.1). The TOMS-OMI data cover the period from 1987 to the present.

However, to infer information about aerosol concentrations, and examine their indirect radiative effects from satellite measurements, significant efforts are needed to acquire more accurate data about particle properties. Satellite remote sensing is not sensitive to particles much smaller than 0.1 micrometer in diameter. Thus, even over vegetated land and dark water, where retrievals are most reliable, the accuracy of the AOD obtained from satellites remote sensing is still much poorer than that obtained from ground-based sun photometers (0.01 to 0.02). The key to reducing the uncertainty of the role of clouds, aerosols, and ozone in climate models is to obtain a better understanding and representation of their climate effects. To that end, it is important to (i) improve measurement quality and coverage, (ii) achieve more effective use of measurements to constrain model simulations and test model parameterizations, and (iii) produce more accurate representations of aerosols and clouds in climate models [55].

Chapter 2

Instruments

2.1 Ground Measurements

From retrieved information about aerosol microphysical properties, one can distinguish anthropogenic aerosols from natural aerosols and also estimate the anthropogenic component of the aerosol direct radiative forcing [56, 57]. Even more accurate information of aerosol properties is needed to infer indirect aerosol radiative forcing effects [58]. For this purpose, measurements with good quality and wide coverage are needed.

2.1.1 AERONET

The worldwide AERONET program (http ://aeronet.gsfc.nasa.gov), which started in 1993, operates a ground-based network of sun and sky radiometers. Routine observations are performed by programable sun/sky radiometers. The spectral measurements of the radiometers are well-calibrated and screened to be cloud-free and quality-assured [59–61]. The accuracy of the aerosol optical thickness (AOT) derived from AERONET measurements at mid-visible wavelengths is in the range from 0.01 to 0.02 [59, 62].

The CIMEL sun/sky radiometers (see Figure 2.1) [63], which are used for measurements in the AERONET program, are solar-powered, automated robot systems with two collimators, each having approximately 1.2° full-angle field of view, one for direct sun radiance measurements and the other for sky radiance measurements. The spectral filters of the radiometers are typically centered at 440, 675, 870, 940, 1,020 nm, and they are located in a motor-driven filter wheel. The real time operation of data acquisition and motion steering is controlled by two microprocessors that are built into an electronic control box.

By use of stepping motors in azimuth and zenith directions with a precision of 0.05° the radiometers are first pointed towards the sun with an accuracy of approximately 1° for direct radiance measurements. The microprocessor computes the position of the sun based on high precision inputs of time, latitude, and longitude, and a 4-quadrant detector is employed for accurate sun tracking. Sky radiances are measured by "Almucantar" scanning and scanning in the "Principal Plane". Figure 2.2 shows the scanning geometries of the CIMEL sun/sky radiometers. These measurements include a large

Figure 2.1: *CIMEL instrument used in AERONET program* [63].

range of scattering angles away from direction of the sun in order to retrieve the AOT, the aerosol size distribution, and the scattering phase function. On clear days, a sequence of measurements of both the direct sun radiance and the sky radiance can be performed automatically 6 times. The measurements are canceled if the "wetness sensor" of the sun photometer is exposed to precipitation. The measured data from the memory of the radiometers can be transferred to a PC or via the Data Collection System (DCS) of AERONET to one of three geostationary satellites: GOES, METEOSAT or GMS, and then transmitted from the satellite to the ground receiving station [59].

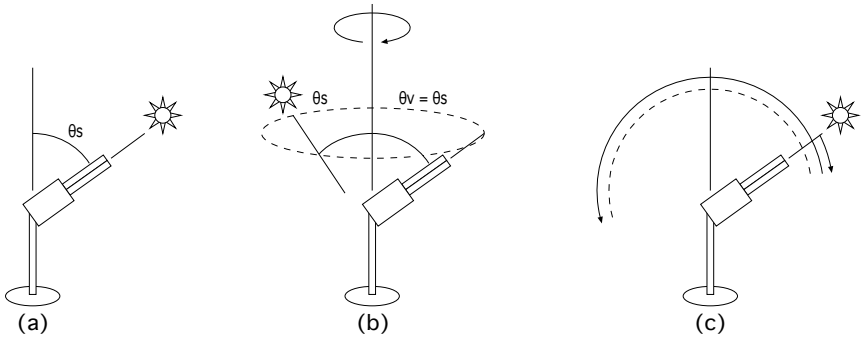

Figure 2.2: *The three different measurement protocols of CIMEL instrument. (a) Sun, (b) Almucantar, and (c) Principal Plane.*

Inversion algorithms to derive effective, column-mean properties have been developed for application to AERONET data in order to retrieve the optical thickness, the single-scattering albedo, size distributions, bimodal fractions, scattering phase functions, and asymmetry factors of aerosols [64–67].

2.1.2 NILU-UV

The NILU-UV instrument has six wavelength channels, and is designed to measure the hemispherical irradiance on a flat surface (see Figure 2.3) [68]. Five of the channels are in the UV spectral range with center wavelengths at 305, 312, 320, 340, and 380 nm, each with a bandwidth of about 10 nm FWHM (Full-Width-at-Half-Maximum). The sixth channel covers wavelengths in the visible range, i.e. between 400 and 700 nm. The data logger of the NILU-UV instrument records one-minute averages every minute. A description of instrument performance is given in [69], and the methodology of data analysis is described in [70]. This method of data analysis is referred to in GAW report No. 190, in section 6.1.2 for calculating biologically effective irradiance, in section 6.3.1 for calculating total ozone column, and in section 6.4 for calculating cloud optical depth [71]. The NILU-UV is temperature stabilized at 50°C, waterproof, and suitable for deployment in harsh environments.

Figure 2.3: *The influence of factors on the climate from year 1750 to year 2005* [68].

We have simulated the error caused by the non-ideal cosine response of the NILU-UV instrument on irradiances at 340 nm for a pure Rayleigh scattering atmosphere and a site altitude of 4,000 m. In the radiative transfer simulations the direct and diffuse radiation components were treated separately. Details about the methodology can be found in [69]. For a SZA of 5° the instrument was found to overestimate the 340 nm irradiance by 1%, while the largest deviation from an ideal cosine response was found for a SZA of 73° with an underestimation of 3%. For situations with overcast sky the errors are expected to be smaller because the direct solar beam is absent. The results presented in this thesis (Chapter 6) have not been corrected for these rather small errors.

For each channel of the instrument NILU-UV instrument, one can apply lamp calibration results taken at regular intervals to calculate a drift factor, which accounts for

the degradation of the optical components, among which the interference filters are the most critical ones.

If the surface at a site where an instrument is placed to measure the hemispherical irradiance, is not flat, obstructions can be accounted for by carrying out radiative transfer simulations. Dahlback et al. [72] estimated a 10° obstruction above a perfect horizon to give a reduction of the measured irradiance by about 3%. In this thesis (Chapter 6), we have estimated the corresponding reduction for a 5° obstruction to be only about 0.7%. The results presented in this thesis have not been corrected for such errors.

2.2 Satellite Measurements

2.2.1 TOMS-OMI

The Total Ozone Mapping Spectrometer (TOMS) and the Ozone Monitoring Instrument (OMI) are instruments deployed on satellites by the NASA project "Ozone and Air Quality" to measure spectral radiance data from which information about atmospheric ozone can be retrieved. Both of these instruments measure data from which one can derive the total ozone column amount (TOCA) as well as other atmospheric parameters related to ozone chemistry and climate. TOMS provided ozone related data from 1978 to 2005, from instruments deployed on three satellites in different periods: Nimbus-7 (November 1978 to June 1993), Meteor-3 (August 1991 to November 1994), and Earth Probe (July 1996 to December 2005) [73].

OMI was launched in July 2004 onboard the Aura satellite, and started providing data in October 2004, thus continuing the TOMS record of TOCA values. There is a data gap from 2002 until OMI started to provide data in October 2004. During this time gap, a latitude dependent error appeared on the measured data from TOMS onboard the Earth Probe satellite, which could not be solved by applying a simple calibration correction. The OMI instrument employs a hyperspectral imaging technique which improves observations of solar backscatter radiation in the visible and ultraviolet spectral regions [73]. From OMI data one can retrieve more atmospheric constituents [74] than from TOMS data, and from OMI data one can differentiate between aerosol types, such as smoke, dust, and sulfates with accuracy and precision unlike that obtained from TOMS data [75], which can not be used to distinguish well between UV-absorbing and non UV-absorbing aerosols.

In this thesis (Chapter 6), we used the TOMS-OMI retrieval algorithm (Version 8.5) to derive TOCA values from OMI data [76]. The algorithm for ozone retrieval only used radiances at 2 wavelengths (317.5 and 331.2 nm under most conditions, and 331.2 and 360 nm for high ozone concentrations and high solar zenith angles). Radiances at longer wavelengths (342.5 and 388 nm for UV-absorbing aerosols; 388 and 483.5 nm for non UV-absorbing aerosols) are used to retrieve aerosol and cloud properties and to estimate column amounts of several trace gases (OClO, BrO, HCHO, NO_2). Radiances at wavelengths shorter than 340 nm, which are heavily absorbed by ozone, are used to

derive total ozone. These algorithms are discussed in OMI Algorithm Theoretical Basis Documents (ATBDs), which are available at $http://eospso.gsfc.nasa.gov/$. The AI (aerosol index) primarily provides a measure of the absorption of UV radiation by smoke and desert dust.

Figure 2.4 shows spring averages of TOCAs over Antarctica measured by ground and satellite instruments, where one can see the difference between TOCA values derived from ground and satellite data. Red dots represent the data from Halley Research Station at Antarctica, while the green and blue dots represent the data from satellite instruments, TOMS and OMI, respectively [28].

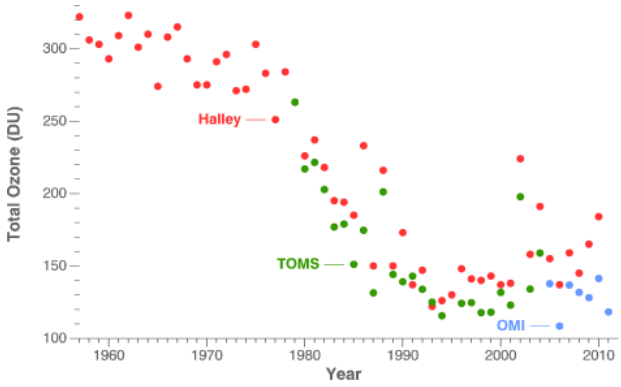

Figure 2.4: *TOCA values over Antarctica (South Pole) measured by ground instruments (red dots) and satellite instruments (green and blue dots)* [28].

Chapter 3

Radiative Transfer Model

3.1 C-DISORT

In this thesis, a radiative transfer (RT) code based on the multiple-stream, multiple scattering DIScrete Ordinate Radiative Transfer model (DISORT) [77] was used for radiative transfer computations. This RT code, C-DISORT, applies to a *coupled* system, such as an atmosphere-ocean system or an atmosphere-snow-ice-ocean system, for use by researchers in the ocean optics, climate research, and remote sensing communities. The C-DISORT code allows for a user-specified number of layers in the coupled system to adequately resolve the vertical variation in the inherent optical properties (IOPs), and it computes apparent optical properties (AOPs), such as upward and downward irradiances, scalar irradiances, and diffuse attenuation coefficients at user-specified optical depths in the coupled system. It also computes radiances in user-specified directions at user-specified optical depths in the coupled system [78, 79]. The scalar RF code used in this thesis ignores polarization effects.

3.2 Light properties

According to the classical physics description, light consist of transverse electromagnetic waves. The full electromagnetic spectrum ranges from very short gamma rays ($\lambda \leq 10$ nm) to very long radio waves ($\lambda \geq 100$ km), whereas visible light covers the wavelength range 400 to 700 nm. When light propagates in a turbid medium through matter, it is attenuated along the propagation direction $\hat{\Omega}$ due to absorption and scattering. In the absence of multiple scattering, the intensity or radiance of light $I_\nu\left(s,\hat{\Omega}\right)$ can be defined by an integral from of the *The Extinction law* [80]

$$I_\nu\left(s,\hat{\Omega}\right) = I_\nu\left(0,\hat{\Omega}\right) e^{-\tau_s(\nu)}. \tag{3.1}$$

Here ν is the frequency of light, and τ_s, which is the extinction optical path or opacity along the path of length s, is given by

$$\tau_s(\nu) = \int_0^s k(s)ds \tag{3.2}$$

where k is the extinction coefficient [m^{-1}], which is equal to the sum of the absorption coefficient $\alpha(s)$ [m^{-1}] and the scattering coefficient $\sigma(s)$ [m^{-1}] of the medium.

3.2.1 Absorption and Scattering

The extinction coefficient $k(s)$, absorption coefficient $\alpha(s)$, and the scattering coefficient $\sigma(s)$ are defined as [80]

$$k(s) = \frac{1}{I^i}\left(\frac{dI^k}{ds}\right) \tag{3.3}$$

$$\alpha(s) = \frac{1}{I^i}\left(\frac{dI^\alpha}{ds}\right) \tag{3.4}$$

$$\sigma(s) = \frac{1}{I^i}\left(\frac{dI^\sigma}{ds}\right). \tag{3.5}$$

where $k(s) = \alpha(s) + \sigma(s)$ [m^{-1}] and I^i is the incident radiance entering a volume element $dV = dA\,ds$ of the medium of cross sectional area dA and propagating the distance ds. dI^k, dI^α, and dI^σ are respectively the radiances that are extinguished (attenuated), absorbed, and scattered in all directions as the light propagates the distance ds.

Absorption of light means that the electromagnetic energy of the incident light is transformed to other forms of energy, for example, to heat. Thus, when a photon of light interacts with an atom with a natural frequency that is close to the frequency of the photon, the electrons of that atom will be excited and enter into a natural vibrational motion, and it will interact with neighboring atoms in such a way as to convert this vibrational energy into thermal energy. In a homogenous medium, such as bulk matter of a pure liquid or solid, absorption is the dominant mode of attenuation. If there is no scattering so that $\sigma(s) = 0$, the exponential attenuation of the irradiance of light is only due to absorption ($I = I_0 e^{-\alpha s}$, where I_0 is the irradiance at $s = 0$). The absorption of light depends on the wavelength of light and on the imaginary part n' of the refractive index of the bulk matter ($\alpha(s) = 4\pi n'/\lambda$) [81]. However, in most cases, absorption and scattering occur simultaneously.

Scattering is the form of propagating energy which is scattered by small particles suspended in a medium. Scattering changes not only the photon's direction but also its radiance, since energy is lost from an incident beam when radiation is scattered. When a photon is introduced into a pencil of radiation and has only one encounter with a particle, the process is called *single scattering*, whereas the term *multiple scattering* is used when several encounters are involved.

The *single-scattering albedo*, defined as

$$a(s) = \frac{\sigma(s)}{\alpha(s) + \sigma(s)} \tag{3.6}$$

is the ratio of the scattering coefficient to the extinction coefficient ($k(s) = \alpha(s) + \sigma(s)$). It represents the fraction of radiation lost by scattering out of a pencil of radiation. If $a = 1$, there is no absorption, i.e. $\alpha(s) = 0$.

The angular distribution of the scattering is described by the scattering phase function $p(s, \cos\Theta)$, while the scattering coefficient $\sigma(s)$ describes its magnitude. The scattering phase function may be defined as follows

$$p(s,\cos\Theta) = 4\pi \frac{\beta(s,\cos\Theta)}{\int_{4\pi}\beta(s,\cos\Theta)d\omega} = \frac{\beta(s,\cos\Theta)}{\frac{1}{2}\int_{-1}^{1}\beta(s,\cos\Theta)d(\cos\Theta)} \tag{3.7}$$

so that

$$\frac{1}{4\pi}\int_{4\pi} p(s,\cos\Theta)d\omega = 1. \tag{3.8}$$

Here $p(s,\cos\Theta)d\omega/4\pi$ is the probability that a photon traveling in the direction $\hat{\Omega}'$ is scattered into a cone of solid angle $d\omega$ around the direction $\hat{\Omega}$ within the volume element dV with thickness ds along $\hat{\Omega}'$.

If we average the cosine of the scattering angle Θ over all scattering directions (weighted by $p(s,\cos\Theta)$), we find

$$\begin{aligned} g &= \langle\cos\Theta\rangle = \frac{1}{4\pi}\int_{4\pi} p(s,\cos\Theta)\cos\Theta\, d\omega \\ &= \frac{1}{2}\int_0^{\pi} p(s,\cos\Theta)\cos\Theta\sin\Theta\, d\Theta = \frac{1}{2}\int_{-1}^{1} p(s,\cos\Theta)\cos\Theta\, d(\cos\Theta). \end{aligned} \tag{3.9}$$

The average cosine g is called the *asymmetry factor* of the scattering phase function, which is a convenient measure of the "shape" of the distribution of the scattered radiation. If $g = 1$, we have complete forward scattering; if $g = -1$, we have complete backward scattering; and if $g = 0$, then either $p(s,\cos\Theta) = 1$ (isotropic scattering) or $p(s,\cos\Theta)$ is symmetric around $\Theta = \pi/2$ (Rayleigh scattering).

Dust, pollen, smoke, water droplets, and other particles in the lower portion of the atmosphere are common causes of *Mie scattering*, which occurs when the particles causing the scattering are larger than the wavelength of radiation. Strictly speaking, Mie scattering describes scattering of electromagnetic radiation by a sphere of any size compared to the wavelength, but this term is often used to describe also scattering by non-spherical particles that are larger than the wavelength. The Henyey-Greenstein (HG) scattering phase function [82] is a common practical approximation to the scattering phase function for large particles:

$$p(\cos\Theta) = \frac{1-g^2}{(1+g^2-2g\cos\Theta)^{3/2}} \tag{3.10}$$

where the parameter g is the asymmetry factor defined in Eq. (3.9). The HG scattering phase function has no physical basis, but is very useful for describing a highly scattering medium, when the actual scattering phase function is unknown. It has the

convenient property that when it is expanded in a series of Legendre polynomials, the the ℓ^{th} expansion coefficient is just the asymmetry factor raised to the power ℓ. [80]

The scattering of light by aerosols is usually responsible for the white-grey haze that one typically sees above polluted cities, while *Rayleigh scattering* (the scattering of light by air molecules) is responsible for the blue color of the sky and the red-orange colors at sunrise or sunset. Rayleigh scattering mainly consists of scattering from atmospheric gases, and can be explained as scattering by spherical particles that are smaller in size than the wavelengths of radiation (the particle should be at least 1/10 smaller than the wavelength). For very small spherical particles, the scattering has the same behavior as for an oscillating dipole, and the amount of scattering increases as the wavelength decreases, so that it becomes proportional to λ^{-4}. For Rayleigh scattering, the scattering phase function is given by

$$p(\cos\Theta) = \frac{3}{4}(1+\cos^2\Theta) \tag{3.11}$$

and the asymmetry factor g is zero since the scattering phase function is symmetric around $\Theta = \pi/2$.

The Rayleigh scattering phase function for unpolarized light is given by

$$p(\cos\Theta) = \frac{3}{3+\tilde{f}}(1+\tilde{f}\cos^2\Theta) \tag{3.12}$$

where the parameter $\tilde{f}$ is the depolarization factor, describing the effects of molecular anisotropy [83–85]. This scattering phase function was originally derived for light scattering by an electric dipole [86]. When unpolarized light of orthogonal polarizations induce dipole moments of the same magnitude, one obtains Eq. (3.12) with $\tilde{f} = 1$. Then the scattered radiation is totally polarized in the observation direction $\Theta = \pi/2$ with polarization direction perpendicular to the scattering plane (the plane spanned by the incident direction and the observation direction). When the two induced dipole moments are not equal, e.g. due to scattering by anisotropic molecules, such as N_2 and O_2, $\tilde{f}$ deviates from 1, and the scattered light at $\Theta = \pi/2$ due to incident unpolarized light, is no longer 100% polarized.

3.3 Radiative transfer equation

The optical depth τ is an important quantity in radiative transfer (RT) theory. The reciprocal extinction coefficient $1/k$ gives the photon mean free path, which is the distance over which a photon travels before it is removed from the pencil of the beam of radiation. Thus, τ gives the number of photon mean free paths. Thus, the optical depth τ gives an estimate of how far one can 'see' into a turbid medium, and for a vertically stratified medium, it is defined as

$$\tau(z) = -\int_z^\infty [\alpha(z') + \sigma(z')]dz' \tag{3.13}$$

where z is the distance in the the vertical direction, which is taken to increase upwards. The absorption coefficient $\alpha(z)$ and the scattering coefficient $\sigma(z)$ are defined in Eqs. (3.4) to (3.5). The negative sign in Eq. (3.13) appears because z is assumed to increase in the upward direction, while τ is taken to increase in the downward direction.

The diffuse radiance distribution $I(\tau,\mu,\phi)$ in a medium can be described by the radiative transfer equation (RTE)

$$\begin{aligned}\mu\frac{dI(\tau,\mu,\phi)}{d\tau} &= I(\tau,\mu,\phi)-S^*(\tau,\mu',\phi')\\ &- \frac{a(\tau)}{4\pi}\int_0^{2\pi}d\phi'\int_{-1}^{1}p(\tau,\mu',\phi';\mu,\phi)I(\tau,\mu',\phi')d\mu'. \qquad (3.14)\end{aligned}$$

In a vertically stratified medium, μ is the cosine of the polar angle θ, ϕ is the azimuth angle, $a(\tau)$ is the single-scattering albedo, as defined in Eq. (3.6), and $p(\tau,\mu',\phi';\mu,\phi)$ is the scattering phase function defined by Eq. (3.7). The differential vertical optical depth is [see Eq. (3.13)]

$$d\tau(z) = -[\alpha(z)+\sigma(z)]dz = -k(z)dz. \qquad (3.15)$$

When we consider a *coupled* system consisting of two adjacent slabs separated by a plane, horizontal interface across which the refractive index changes abruptly from a value m_1 (complex refractive index $m_1 = n_1 + in_1'$) in slab$_1$ to a value m_2 (complex refractive index $m_2 = n_2 + in_2'$) in slab$_2$, the single-scattering source term $S^*(\tau,\mu',\phi')$ in Eq. (3.14) is given by the following expressions in slab$_1$ and slab$_2$ [87]

$$\begin{aligned}S_1^*(\tau,\mu,\phi) &= \frac{1}{4\pi}a(\tau)F^0p(\tau,-\mu_0,\phi_0;\mu,\phi)e^{-\tau/\mu_0}\\ &+ \frac{1}{4\pi}a(\tau)F^0\rho_F(-\mu_0;m_1,m_2)p(\tau,\mu_0,\phi_0;\mu,\phi)e^{-(2\tau_1-\tau)/\mu_0} \qquad (3.16)\end{aligned}$$

$$\begin{aligned}S_2^*(\tau,\mu,\phi) &= \frac{1}{4\pi}a(\tau)F^0\frac{\mu_0}{\mu_{0n}}\mathcal{T}_F(-\mu_0;m_1,m_2)\\ &\times\ p(\tau,-\mu_{0n},\phi_0;\mu,\phi)e^{-\tau_1/\mu_0}e^{-(\tau-\tau_a)/\mu_{0n}} \qquad (3.17)\end{aligned}$$

where F^0 is the intensity of incident light beam from the direction $(-\mu_0,\phi_0)$, τ_1 is the vertical optical depth of the upper slab, $\rho_F(-\mu_0;m_1,m_2)$ in Eq. (3.16) is the Fresnel reflectance at the slab$_1$-slab$_2$ interface and $\mathcal{T}_F(-\mu_0;m_1,m_2)$ in Eq. (3.17) is the Fresnel transmittance through the interface. μ_0 is the cosine of the zenith angle of the incident beam of illumination θ_0 ($\mu_0 = \cos\theta_0$), and where $n_2 > n_1$. μ_{0n} is the cosine of the polar angle θ_{0n} in slab$_2$, which is related to $\theta_0 = \arccos\mu_0$ by Snell's law. In slab$_1$, the single-scattering source term consists of first-order scattering of the attenuated incident beam and first-order scattering of the attenuated incident beam that is reflected at the slab1-slab2 interface., and in slab$_2$ it consists of the attenuated incident beam that is refracted through the interface.

The Fresnel reflectance at the slab$_1$-slab$_2$ interface is given by [87]

$$\rho_F = \frac{1}{2}\left[\left|\frac{\mu_i - m_r\mu_t}{\mu_i + m_r\mu_t}\right|^2 + \left|\frac{\mu_t - m_r\mu_i}{\mu_t + m_r\mu_i}\right|^2\right] \tag{3.18}$$

where $\mu_i = \cos\theta_i$, θ_i is the angle of incidence, $\mu_t = \cos\theta_t$, θ_t is the angle of refraction determined by Snell's law ($n_1 \sin\theta_i = n_2 \sin\theta_t$), and $m_r = m_2/m_1$.

The Fresnel transmittance through the interface is given by [87]

$$\mathcal{T}_F = 2\mu_i\mu_t\left[\left|\frac{1}{\mu_i + m_r\mu_t}\right|^2 + \left|\frac{1}{\mu_t + m_r\mu_i}\right|^2\right]\frac{n_2}{n_1}. \tag{3.19}$$

If we isolate the azimuth dependence from the RTE by expanding the radiance in a Fourier cosine series, and expanding the scattering phase function in *Legendre polynomials*, we find that each Fourier component I^m of the radiance satisfies the the following RTE [80].

$$\begin{aligned}\frac{dI^m(\tau,\mu)}{d\tau} &= I^m(\tau,\mu) - S^{*m}(\tau,\mu) \\ &\quad -\frac{a(\tau)}{2}\int_{-1}^{1} p^m(\tau,\mu',\mu)\, I^m(\tau,\mu)\, d\mu\end{aligned} \tag{3.20}$$

where $m = 0, 1, 2, \ldots, 2N-1$, and where $p^m(\mu',\mu)$ is obtained by expanding the scattering phase function in *Legendre polynomials*, i.e.

$$p^m(\mu',\mu) = \sum_{l=m}^{2N-1}(2l+1)\chi_l\Lambda_l^m(\mu')\Lambda_l^m(\mu). \tag{3.21}$$

Here $\chi_l = \frac{1}{2}\int_{-1}^{1} d(\cos\Theta)P_l(\cos\Theta)p(\cos\Theta)$ is an expansion coefficient and $\Lambda_l^m(\mu)$ is given by

$$\Lambda_l^m(\mu) = \sqrt{\frac{(l-m)!}{(l+m)!}}\, P_l^m(\mu) \tag{3.22}$$

where $P_l^m(\mu)$ is an associated Legendre polynomial of order m.

For a discrete ordinate approximation, the downward irradiance in slab$_1$ consists of a direct component E_{dir}^1 and a diffuse component $E_{d,diff}^1$, given by [87]

$$E_{dir}^1(\tau) = \mu_0 F^0 e^{\tau/\mu_0} \tag{3.23}$$

$$E_{d,diff}^1(\tau) = 2\pi\int_0^1 \langle I_{d,diff}^1(\tau,\mu)\rangle\,\mu\, d\mu \tag{3.24}$$

where $\langle I_{d,diff}^1(\tau,\mu)\rangle$ is the azimuthally-averaged diffuse downward radiance at optical depth $\tau \le \tau_1$ in slab$_1$.

The upward diffuse irradiance $E^1_{u,diff}$ in slab$_1$ is given by [87]

$$E^1_{u,diff}(\tau) = 2\pi \int_0^1 \langle I^1_{u,diff}(\tau,\mu)\rangle \mu \, d\mu. \tag{3.25}$$

The downward and upward irradiances in slab$_2$ are [87]

$$E^2_{dir}(\tau) = \mu_0 F^0 e^{[-\tau_1/\mu_0 - \tau/\mu_{0n}]} \tag{3.26}$$

$$E^2_{d,diff}(\tau) = 2\pi \int_0^1 \langle I^2_{d,diff}(\tau,\mu)\rangle \mu \, d\mu \tag{3.27}$$

$$E^2_{u,diff}(\tau) = 2\pi \int_0^1 \langle I^2_{u,diff}(\tau,\mu)\rangle \mu \, d\mu \tag{3.28}$$

where the downward and upward azimuthally-averaged radiances in slab$_2$ are given by $\langle I^2_{d,diff}(\tau,\mu)\rangle$ and $\langle I^2_{u,diff}(\tau,\mu)\rangle$, respectively.

The numerical code C-DISORT computes radiances at any optical depth, polar, and azimuth angle by solving the RTE in Eq. (3.20) for each layer of the two slabs by using the discrete-ordinate method to convert the integro-differential RTE into a system of coupled ordinary differential equations.

The C-DISORT method can be summarized as follows:

1. Slab$_1$ (complex refractive index $m_1 = n_1 + in'_1$) and slab$_2$ (complex refractive index $m_2 = n_2 + in'_2$) are separated by a plane interface at which the refractive index changes from m_1 in slab$_1$ to m_2 in slab$_2$, where m_2 depends on the wavelength.

2. Each of the two slabs is divided into a sufficiently large number of horizontal layers, each assumed to be homogenous, to resolve the vertical variation of its IOPs.

3. Fresnel's equations for the reflectance and transmittance are applied at the interface between the two slabs, and the Law of Reflection and Snell's Law are used to determine the directions of the reflected and refracted rays.

4. In each of the two slabs, discrete-ordinate solutions to the RTE are calculated separately for each homogeneous layer.

5. Boundary conditions at the top of slab$_1$ and the bottom of slab$_2$ and continuity conditions at layer interfaces within each of the two slabs are applied.

Chapter 4

Further applications

In order to reduce uncertainties in the understanding of the climate system due to radiative forcing by clouds and aerosols, one may use observations from satellites, which provide both temporal and global information about the atmospheric impact on the radiative forcing. But it is very difficult to separating the contributions from the surface and the atmosphere to the radiation measured by a satellite instrument. Several different retrieval algorithms and satellite instruments (such as MODIS [43–45], MERIS [46–48], and MISR [49, 50]) are currently being used to help distinguish the surface contribution from the atmospheric contribution [51]. These retrieval algorithms were developed by using large amounts of data from ground instruments combined with radiative transfer calculations. Therefore, high accuracy of ground measurements covering a wide surface range is a precondition for constructing accurate retrieval algorithms, especially in order to reduce uncertainties of radiative forcing by clouds and aerosols, since the level of understanding of their impact on the climate system is still low. A further application of the results in this thesis is to develop retrieval algorithms that can be used in remote sensing of coupled atmosphere-surface systems. Features of some past and current satellite instruments as well as instruments planned to be launched in the future for remote sensing purposes are discussed below.

4.1 MODIS

MODerate resolution Imaging Spectroradiometer (MODIS) instruments were installed on the satellite platforms Terra in 2000 and Aqua in 2002 [55]. MODIS provides daily, global coverage over land and ocean areas of the loading as well as the size and shape of aerosols, estimated from TOA radiance measurements in 36 spectral bands in the region 0.41–14 μm (see 4.1 [88]). The spatial resolution of MODIS measurements is 0.5 x 0.5 km^2 at 0.55 μm [54]. The retrieved aerosol parameters include the aerosol optical depth τ_a, the Angstrom exponent α, the effective radius r_{eff}, the asymmetry factor g, and the fine-mode fraction f (fraction of small particles vs. large particles). MODIS retrieves τ_a at 7 visible and near infrared (NIR) channels in the solar spectral region from 0.47 to 2.1 μm over land with a high accuracy of $0.05 \pm 0.20\tau_a$ [89, 90], and over ocean with an even higher accuracy of $0.03 \pm 0.05\tau_a$ because of the greater simplicity of the ocean surface [90, 91].

Primary Use	Band	Bandwidth[1]	Spectral Radiance[2]	Required SNR[3]
Land/Cloud/Aerosols Boundaries	1	620 - 670	21.8	128
	2	841 - 876	24.7	201
Land/Cloud/Aerosols Properties	3	459 - 479	35.3	243
	4	545 - 565	29.0	228
	5	1230 - 1250	5.4	74
	6	1628 - 1652	7.3	275
	7	2105 - 2155	1.0	110
Ocean Color/ Phytoplankton/ Biogeochemistry	8	405 - 420	44.9	880
	9	438 - 448	41.9	838
	10	483 - 493	32.1	802
	11	526 - 536	27.9	754
	12	546 - 556	21.0	750
	13	662 - 672	9.5	910
	14	673 - 683	8.7	1087
	15	743 - 753	10.2	586
	16	862 - 877	6.2	516
Atmospheric Water Vapor	17	890 - 920	10.0	167
	18	931 - 941	3.6	57
	19	915 - 965	15.0	250

Primary Use	Band	Bandwidth[1]	Spectral Radiance[2]	Required NE[delta]T(K)[4]
Surface/Cloud Temperature	20	3.660 - 3.840	0.45(300K)	0.05
	21	3.929 - 3.989	2.38(335K)	2.00
	22	3.929 - 3.989	0.67(300K)	0.07
	23	4.020 - 4.080	0.79(300K)	0.07
Atmospheric Temperature	24	4.433 - 4.498	0.17(250K)	0.25
	25	4.482 - 4.549	0.59(275K)	0.25
Cirrus Clouds Water Vapor	26	1.360 - 1.390	6.00	150(SNR)
	27	6.535 - 6.895	1.16(240K)	0.25
	28	7.175 - 7.475	2.18(250K)	0.25
Cloud Properties	29	8.400 - 8.700	9.58(300K)	0.05
Ozone	30	9.580 - 9.880	3.69(250K)	0.25
Surface/Cloud Temperature	31	10.780 - 11.280	9.55(300K)	0.05
	32	11.770 - 12.270	8.94(300K)	0.05
Cloud Top Altitude	33	13.185 - 13.485	4.52(260K)	0.25
	34	13.485 - 13.785	3.76(250K)	0.25
	35	13.785 - 14.085	3.11(240K)	0.25
	36	14.085 - 14.385	2.08(220K)	0.35

[1] Bands 1 to 19 are in nm; Bands 20 to 36 are in μm
[2] Spectral Radiance values are (W/m^2 -μm-sr)
[3] SNR = Signal-to-noise ratio
[4] NE(delta)T = Noise-equivalent temperature difference
Note: Performance goal is 30-40% better than required

Table 4.1: *Spectral bands of MODerate resolution Imaging Spectroradiometer* (MODIS) [88].

Figures 4.1(a) and (b) show the global monthly means over land for September 2000 for τ_a and α, respectively. The most visible dry-season biomass burning is in Africa and in South America with mean τ_a values of about 0.5–0.7 compared to τ_a values with means of about 0.2–0.3 in Europe and North America and 0.4–0.5 in China and India. The boundary of the Sahara Desert with small α values shows a possible mixture of urban/industrial or bio-mass burning aerosols and dust particles [92].

4.2 MERIS

The MEdium Resolution Imaging Spectrometer (MERIS) instrument was installed on the satellite platform ENVISAT, which was launched in 2002 [93]. MERIS has 15 spectral bands in the visible and near infrared (See Table 4.2 [93]) and a spatial resolution of 0.3 x 0.3 km^2 at 0.55 μm, which is better than that of MODIS [93]. MERIS, which was in operation until April 2012, was primary designed to measure *ocean color* of oceans and coastal areas. From measurements of ocean color, one can infer information about the ocean carbon cycle and the thermal regime of the upper ocean, help the management of fisheries and coastal zones, and get information of climate and ocean

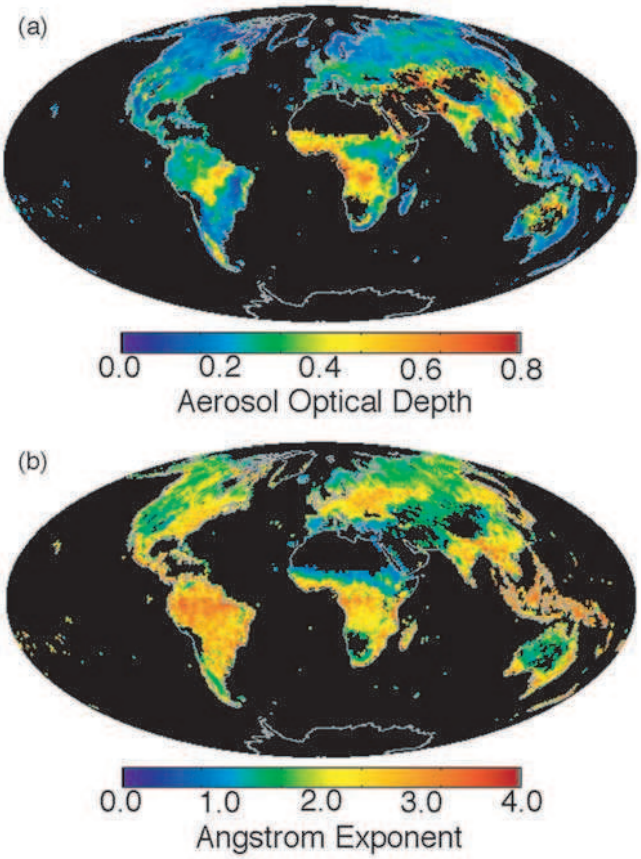

Figure 4.1: *Global monthly mean of (a) the aerosol optical depth τ_{AOD} at 0.55 μm and (b) the Angstrom exponent α derived from MODIS level-3 daily products from September 2000* [92].

dynamics [54, 93]. MERIS can also provide estimates of type, top height, and albedo of clouds, vegetation indices, photosynnthetically available radiation (PAR), surface pressure, water vapor total column content, and aerosol loading over land [93].

Through global observations of ocean color and ocean temperature, MERIS provides a remote sensing capability for observing oceanic biology and marine water quality (Figures 4.2). MERIS can estimates concentrations of phytoplankton, yellow substance, and suspended sediments in the oceans. For the marine water quality, the marine water constituent concentrations and distributions, which are highly affected by human activities, are assessed. The applications of each band of MERIS is listed in Table 4.2 [93].

No.	Band center (nm)	Band width (nm)	Applications
1	412.5	10	Yellow substance and detrital pigments
2	442.5	10	Chlorophyll absorption maximum
3	490	10	Chlorophyll and other pigments
4	510	10	Suspended sediment, red tides
5	560	10	Chlorophyll absorption minimum
6	620	10	Suspended sediment
7	665	10	Chlorophyll absorption & fluorescence reference
8	681.25	7.5	Chlorophyll fluorescence peak
9	708.75	10	Fluorescence reference, atmosphere corrections
10	753.75	7.5	Vegetation, cloud, O_2 absorption band reference
11	760.625	3.75	O_2 R- branch absorption band
12	778.75	15	Atmosphere corrections
13	865	20	Atmosphere corrections
14	885	10	Vegetation, water vapor reference
15	900	10	Water vapor

Table 4.2: *Spectral bands of MEdium Resolution Imaging Spectrometer (MERIS)* [93].

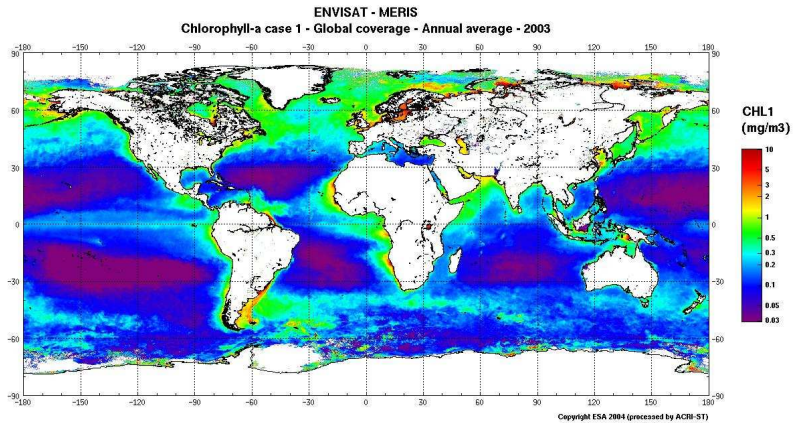

Figure 4.2: *Global ocean color image from MERIS - Annual average 2003* [93].

4.3 SeaWiFs

The Sea-viewing Wide Field-of-view Sensor (SeaWiFS) was installed on the SeaStar spacecraft, which was developed by Orbital Sciences Corporation (OSC) and launched on 1997 [94]. SeaWiFS was a follow-on experiment to the Coastal Zone Color Scanner on Nimbus 7. The operation period of SeaWiFS was from 1997 to 2010. Its purpose was to provide quantitative data on global ocean bio-optical properties to the scientific community from a 705 km (380 nmi) orbital altitude (Figures 4.3). The nadir resolution of SeaWiFs is 1.1 km in LAC (Local Area Coverage) and 4.5 km in GAC (Global Area Coverage).

The chlorophyll product derived from SeaWiFS data is in good agreement with that derived from MERIS data. They differed significantly at 412 and 443 nm, where MERIS was more similar to model calculations and in situ data, implying that SeaWiFS did not provide accurate reflectances (water-leaving radiance) at 412 and 443 nm.

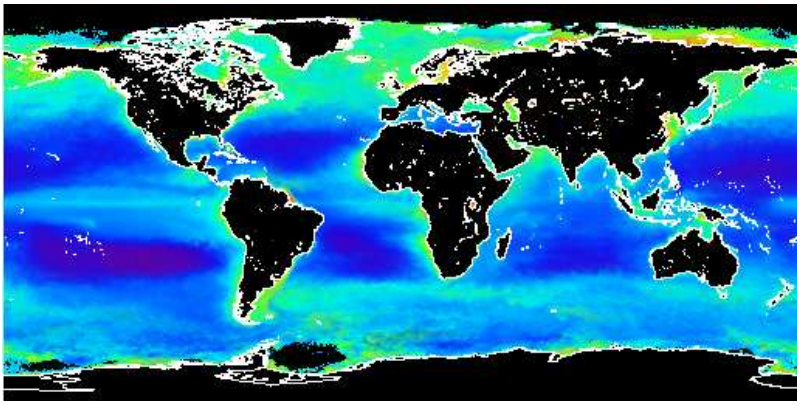

Figure 4.3: *Global ocean color image from SeaWiFS - Annual average 2003* [94].

4.4 MISR

The Multi-angle Imaging SpectroRadiometer (MISR) instrument was installed on the satellite platform Terra, which was launched in 2000 [55]. MISR was designed to improve the understanding of the ecology, environment, and climate on Earth. Global, radiometrically calibrated, geo-rectified, and spatially co-registered imagery can be provided weekly by MISR at nine viewing angles (nadir plus 26.1°, 45.6°, 60.0°, and 70.5° in the forward and aft directions along the flight path) and four visible-near-infrared spectral bands (446, 558, 672, and 867 nm). The novel approach of imaging the Earth in nine different viewing directions makes it feasible to more accurately evaluate the surface contribution to the TOA radiance and impacts of different types of atmospheric particles and clouds on climate regionally and globally [95]. A detail of the 36 channels of MISR is shown in Table 4.3 [96]. The spatial resolution of MISR is 0.275 x 0.275 km^2 or 1.1 x 1.1 km^2, depending on the channel, and aerosol products are derived at a spatial resolution of 17.6 x 17.6 km^2 [54].

Figures 4.4 shows the geographic distribution of MISR retrievals in mixed ocean, land, and cloudy scene in northern Canada [97].

4.5 EarthCARE

The Earth Clouds, Aerosols and Radiation Explorer mission (EarthCARE) is a joint European-Japanese mission aiming to quantify aerosol-cloud-radiation interactions to obtain a better understanding of Earth's climate system. To that end, the radiative interactions between clouds and aerosol processes must be fully investigated.

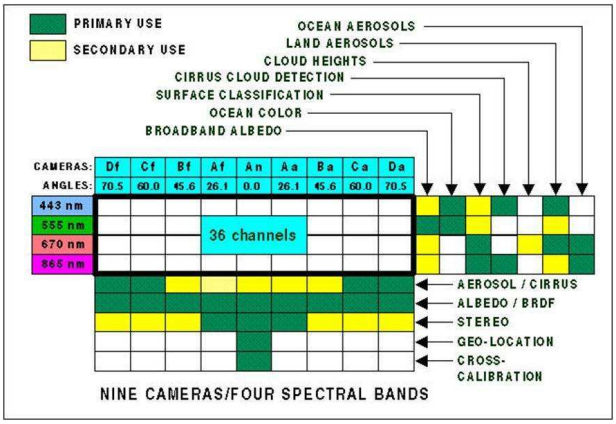

Table 4.3: *36 channels of Multi-angle Imaging SpectroRadiometer (MISR)* [96].

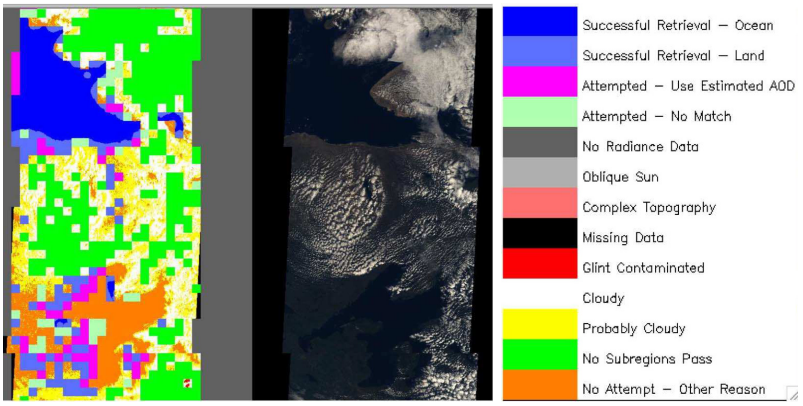

Figure 4.4: *MISR image in mixed ocean, land, and cloudy scene in northern Canada, centered near 67.9 N latitude, 119.2 W longitude. It showing the distribution of retrieval status, with paired nadir-view true-color images* [97].

The scope of the mission is illustrated in Fig. 4.5. The goal is to accurately represent aerosol-cloud-radiation interactions in climate and numerical weather forecasting models on a global scale by providing vertical profiles and radiative properties of natural and anthropogenic aerosols and radiative interactions between aerosols and clouds. This goal is to be reached by providing (i) vertical distribution and radiative impact of atmospheric water and ice, (ii) transport of water and ice by clouds, (iii) characterization of vertical motion within clouds, (iv) vertical profiles of cloud overlap, (v) and cloud-precipitation interactions, and (vi) a combination of retrieved aerosol and cloud properties to derive profiles of atmospheric radiative heating and cooling [98].

4.6 Sentinel

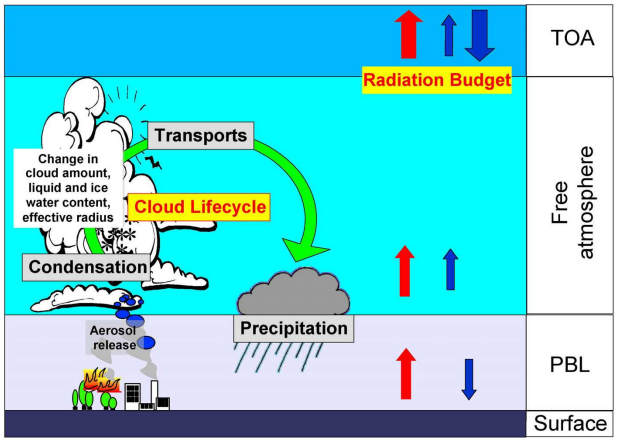

Figure 4.5: *The scope of the EarthCARE mission* [98].

Sentinel is a multi-satellite project to be launched over the next decade, being developed by ESA under the Global Monitoring for Environment and Security (GMES) programme. The Sentinel missions include [99]

- *Sentinel 1*: provides all-weather, day and night radar imaging for land and ocean and sea-ice monitoring (launch in 2013). It has a swath width of 250 km and a ground resolution of 5 x 20 m.

- *Sentinel 2*: provides super-spectral imaging for vegetation, soil and water cover, inland waterways, and coastal areas (launch in 2013). Sensors comprise 13 spectral bands. The spatial resolution of is at 10 m for 4 bands, at 20 m for 6 bands, and at 60 m for 3 bands with a swath width of 290 km.

- *Sentinel 3*: provides ocean and global land monitoring services (launch in 2013). It has a Sea and Land Surface Temperature Radiometer (SLSTR), which is based on ENVISAT's Advanced Along Track Scanning Radiometer (AATSR), for determining global sea-surface temperatures to an accuracy of better than 0.3 K. The spatial resolution of SLSTR in the visible and shortwave infrared channels is 500 m and 1 km in the thermal infrared channels. It includes an Ocean and Land Colour Instrument (OLCI), which will provide a new generation of measurements over the ocean and land, and which is based on heritage from ENVISAT's MERIS. With 21 bands, compared to the 15 bands of MERIS, OLCI has a design optimized to minimize sun-glint, and has a resolution of 300 m over all surfaces. The swath of nadir SLSTR and OCLI has full overlap. A dual-frequency (Ku and C band) advanced Synthetic Aperture Radar Altimeter (SRAL) is based on heritage from CryoSat and provides measurements at a resolution of 300 m in SAR mode along track.

- *Sentinel 4*: provides atmospheric monitoring services, including the monitoring of air quality, stratospheric ozone and solar radiation, and climate monitoring. (Onboard a Meteosat Third Generation Satellite to be launched in 2017 and 2019).

- *Sentinel 5*: provides atmospheric monitoring services of the same type as those provided by Sentinel 4 (Onboard a post-EUMETSAT Polar System (EPS) spacecraft with launch in 2020).
- *Sentinel 5 Precursor*: reduces data gaps (especially SCIAMACHY atmospheric observations) between the ENVISAT and the Sentinel 5 (launch in 2015). The launch of the Sentinel 5 Precursor might be rescheduled since the ENVISAT lost connection with Earth in April 2012.

Figure 4.6 shows a virtual figure of the Sentinel 3, whose orbit provides a 27-day repeat for the topography package, with a 4-day sub-cycle.

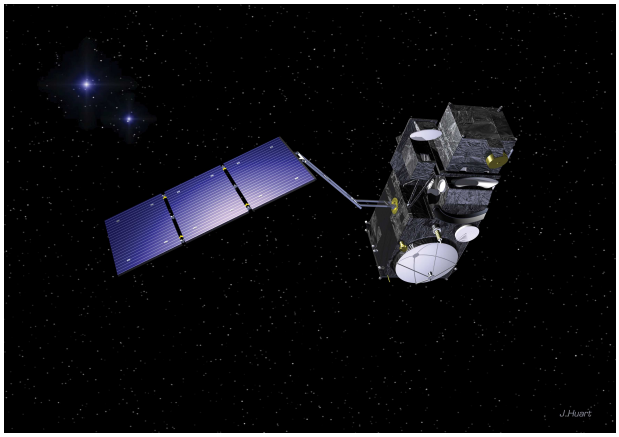

Figure 4.6: *The virtual figure of the Sentinel 3* [99].